Wear Behavior of Biodegradable Mg–5Zn–1Y–(0–1)Ca Magnesium Alloy in Simulated Body Fluid

Asma Ghanbari[1] · Hassan Jafari[2] · Faramarz Ashenai Ghasemi[1]

Abstract

In this study, wear behavior of biodegradable Mg–5Zn–1Y–(0–1)Ca alloys is investigated in simulated body fluid. Wear test is performed using a pin-on-disc system, under three different loads of 10, 20 and 40 N, at ambient temperature; and the whole configuration is exposed to simulated body fluid. The volumetric wear rate and friction coefficient of each alloy are determined. The worn surfaces are analyzed using a scanning electron microscope, equipped with an energy dispersive spectrometer to determine the involved main wear mechanism. The Ca-free alloy contains α-Mg and intermetallic Mg_3YZn_6, and Ca addition produces another intermetallic $Ca_2Mg_6Zn_3$. Results show that different wear mechanisms and rates, as well as friction coefficients, are achieved due to the effect of simulated body fluid on the alloys with regards to the different Ca content and the presence of corrosion products. Microscopic studies reveal that abrasion is the dominant wear mechanism taken place in all alloys under all loads. Increasing Ca content leads to wear resistance deterioration while increasing wear load results in decreasing wear rate and friction coefficient of the alloys. The results of the wear rate and friction coefficient of Mg–5Zn–1Y–1Ca alloy exhibit greater instability compared to the other alloys due to its more enhanced corrosion caused by the formation of the intermetallic $Ca_2Mg_6Zn_3$ particles. In total, Ca-free alloy provides the best wear resistance, especially at the higher wear load.

Keywords Mg alloys · Biodegradation · Wear · Corrosion · Friction coefficient · Simulated body fluid

1 Introduction

Magnesium (Mg) and its alloys are highly potent materials to be considered for biomedical applications due to their excellent mechanical properties, biocompatibility and good osteoconductivity [1]. Their low density (1.78–2 g/cm³) and elastic modulus (41–45 GPa), which are very close to those of natural bone (1.8–2.1 g/cm³ and 3–20 GPa, respectively) are superior and determining keys over other biomedical alloys such as titanium alloys (4.43 g/cm³, 110–117 GPa), stainless steel (7.9 g/cm³, 205–210 GPa) and cobalt–chromium alloys (7.8 g/cm³, 230 GPa) [2]. It is interesting to note that the close elastic modulus of Mg and its alloys to that of natural bone reduces the effect of stress shielding between implants and normal bones [3]. Mg is naturally found in bone tissue and is an essential element of the human body. It has also biodegradability in the body's physiological environments [4, 5]. In particular, Mg^{2+} are present in the human body abundantly and are involved in many metabolic reactions and biological mechanisms [3]. Typically, the body of a human with 70 kg weight, contains about 21–35 g of Mg and needs to be daily fed with 180–350 mg of this element [6, 7]. The high concentrations of Mg^{2+} can lead to the activation of bone cells and increase bone volume around Mg implant [8]. Moreover, despite the degradation of such implants in the body, their corrosion products do not damage the surrounding tissues [8]. Thus, these materials are noticed as orthopedic implants in bone surgery [9] as well as vascular stents [5, 10, 11]. For instance, reports show that biodegradable Mg stents can be useful in immediate access to angiographic results [12].

✉ Hassan Jafari
 jafari_h@yahoo.com; hjafari@sru.ac.ir

1 Faculty of Mechanical Engineering, Shahid Rajaee Teacher Training University (SRTTU), P.O. Box 16785-136, Tehran, Iran

2 Materials Engineering Department, Faculty of Materials Engineering and Modern Technologies, Shahid Rajaee Teacher Training University (SRTTU), P.O. Box 16785-136, Tehran, Iran

For biodegradable orthopedic implants, some specific properties such as proper strength and elastic modulus, suitable corrosion rate and non-toxicity of corrosion products are expected [13]. Therefore, the use of appropriate alloying elements is very important to fulfill the expectation. Zinc (Zn) with the amount of 85% in muscle and bone, 11% in skin and liver, and about 4% in other body tissues is one of the most abundant elements in the human body [14]. It is also involved in the structure and performances of a large number of macromolecules and reactions of more than 300 enzymes [14]. In addition, Zn leakage causes the impairing of DNA synthesis and protein metabolism resulting in negative impacts on bone formation [7]. It improves the corrosion resistance and strength of Mg alloys through solid solution forming [10, 15]. Mg–Zn binary alloy containing 5–6 wt% Zn has been reported to have good corrosion resistance in simulated body fluid [16, 17]. Calcium (Ca) is one of the essential elements of the human body as well as the main component of bone to accelerate bone growth. It plays a key role in chemical signaling of the cells. In particular, the simultaneous releasing of Ca and Mg ions in the body is beneficial to heal bones [7]. Mg–Zn–Ca alloy, due to its good biocompatibility and mechanical properties and non-cytotoxicity, is a suitable choice for biomedical applications [11, 18, 19]. Yttrium (Y), as one of the rare earth elements, can have a beneficial effect on the corrosion resistance and mechanical properties of Mg alloys [20]. Zhang et al. [21] showed that the Mg-Zn–Y alloy has better corrosion properties than AZ31 and AZ91, due to the addition of Y. They believe that the ternary Mg–Zn–Y alloy, due to its suitable properties, can be used for biomedical applications such as bone implants. In addition, it is believed that Mg-Y alloy shows low toxicity for osteoblast [9]. In an investigation on Mg–5Zn–1Y–xCa (x=0–1 wt%) alloys, proper corrosion resistance in the simulated body fluid was reported [22].

However, a major problem encountered during the application of such alloys is comparatively poor anti-wear characteristic when they are used as moving implant parts [23, 24]. When Mg alloys are in contact with parts bearing a load and exposed to a corrosive environment, the mutual wear and corrosion effects are not negligible [25]. It has been shown that, after implantation, apart from corrosion resistance, micro-movement behavior between the implant and bone is undoubtedly observed by in vivo corrosion effect [26]. Therefore, attention to the wear and friction behavior of biomedical candidate alloys is essential. Somekawa et al. [27] studied the wear and frictional properties of Mg–Zn–Y alloy with quasi-crystalline phase dispersion. Their results showed that the homogeneous distribution of the phase in the coarse-grained matrix dramatically increases wear properties of the alloy. The wear behavior study of Mg97Zn1Y2 alloy by An et al. [24] showed that changing microstructure and mechanical properties by raising the surface temperature during dry

sliding can control the wear. Back to the literature, it can be inferred that the wear properties of several commercial Mg alloys used in industry, such as AZ91D [28], AM50B [29], reo-cast AZ91 and AM60B [30], etc. have been investigated. However, few studies have been conducted on the wear and friction behavior of biodegradable alloys, especially in the human body environment. For example, the study of wear properties of Mg–2Zn–0.2Mn [26] and Mg–Zn–Ca [31] showed that wear rate of the alloys in simulated body fluid (SBF) is higher than the dry environment due to the corrosion effect happens in SBF.

In this study, the wear and frictional behavior of Mg–5Zn–1Y–xCa (x=0–1 wt%) alloys have been investigated. Since the implant applications of this alloy are most desirable [22], the investigation on wear properties of the alloy in SBF sufficiently benefits to provide more detailed information on the biomedical application of Mg alloys.

2 Materials and Methods

2.1 Alloys Preparation

Mg–5Zn–1Y–xCa (x=0.0, 0.3, 0.5, 1.0 wt%) alloys were cast from commercial pure grade (99.9%) of Mg, Zn, and Ca ingots and Mg-30Y master alloy by electric resistance furnace (Azar furnaces–VM10L1200). First, Mg ingot was melted in a steel crucible at 750 °C, then the appropriate amount of preheated Mg–30Y master alloy and Zn ingot were added to the molten metal while it was stirring. Finally, different amounts of Ca ingot, with the conditions mentioned for Zn ingot, were added to the prepared molten metal to fabricate the required alloys. Afterward, the molten alloys were heated for another 10 min to homogenize it before pouring into a simple steel mold with the dimensions of $70 \times 50 \times 10$ mm and were left to cool to room temperature in air. It should be noted that due to the high affinity of Mg alloys to oxygen, argon gas (99.99%) flow was utilized to protect the molten metal from oxidation at all stages of melting and pouring processes.

2.2 Chemical Composition Analysis and Microstructure Characterization

The chemical composition of the cast alloys was measured by inductively coupled plasma atomic emission spectroscopy (ICP–AES). Samples with the size of 15 mm $\times 10$ mm $\times 10$ mm were cut, machined, then ground with SiC papers up to a final of 5000 grit. Afterward, the prepared specimens were polished using diamond paste with the size of 6 μm, and finally etched with 10% Nital (10 ml nitric acid + 100 ml ethanol) for 5 s to reveal microstructure. Scanning electron microscope (FEI ESEM Quanta 200)

equipped with an energy dispersive X–ray spectroscopy (EDS, Silicon drift 2017) was used to observe the microstructure of the alloys. X–ray diffraction (XRD) was used to analyze the phases present in the microstructure of alloy using the Yonissantis dispersive device (XMD–300) on a polished bulk sample at a range of 10° to 90°. The analysis was used with the X–ray light bulb with 45 kV and the copper anode producing CuK_α radiation with a wavelength of 1/541874 °A and nickel as the filter. X'pert HighScore plus (2.2b version) was used to interpret the results.

2.3 Wear Test

The wear tests were performed in SBF, based on the ASTM G99 standard, using a pin-on-disc machine at room temperature. The chemical materials and preparing method of SBF can be found in Ref. [32]. The pins of wear test with a diameter of 5 mm and a length of 30 mm were cut from the cast alloys using a wire cut electrical discharge machine (Charmilles Robofil 200). The contact surface of the pins was ground up to 5000 grit SiC papers and then cleaned by ethanol and dried using warm air before the test. The counter-face disc with a diameter of 40 mm, cut from an ASTM A295 bearing steel (grade 52100), was austenitized at 850 °C for 45 min, then quenched in oil to obtain a hardness of 64 HRC, and finally was gently ground with different SiC papers up to 1000 grit. The path length and disc speed were considered 100 m and 30 rpm, respectively, calculating a constant speed of 0.03 m/s under three different loads of 10, 20 and 40 N for the wear test. The pins and disc were ultrasonically cleaned in acetone before wear test, washed and dried to avoid any probable contamination. The friction coefficient was continuously reported using an attached computer. In each wear test, the pin was weighed using a digital scale with a precision of ± 0.0001 gr for an interval of 20 m. After each step, the pin was cleaned in boiling CrO_3 solution (200 g/L) for 5 min in order to remove corrosion products [11, 18] before weighing. Equation (1) [33] was used to calculate the volumetric wear rate.

$$W_r = \frac{m}{\rho l F} \tag{1}$$

where W_r is the volumetric wear rate, m is the mass loss, ρ is the density of the alloy, l is the traveled distance and F is the

normal load. Each test was repeated thrice to provide reliable data, and an average result was reported. The surface area of wear zone on each pin was measured by the ImageJ software (1.40 g version), and the worn surfaces were analyzed using SEM/EDS to study the wear mechanism.

3 Results

3.1 Chemical Composition of the Cast Alloys

The chemical composition of the alloys is presented in Table 1. The values indicate that the alloys are in the range of the nominal composition of the Mg–5Zn–1Y alloy having different percentages of calcium (0.3, 0.5 and 1).

3.2 Microstructural Analysis

Figure 1 show SEM images of the microstructure of the cast Mg–5Zn–1Y–xCa alloys. As can be seen, the microstructures consist of the matrix and some continuous and discontinuous secondary intermetallics located at the grain boundaries and interdendritic regions, respectively. The EDS results, shown in Table 2, represent that, apart from α-Mg (the matrix, Point A), two different intermetallics denoted as B and C are rich in Y and Ca, respectively. The XRD results, shown in Fig. 2, confirm that the cast Mg–5Zn–1Y–xCa alloy, consists of α-Mg, Mg_3YZn_6, and $Ca_2Mg_6Zn_3$. The results are reported by other researchers as well [19, 24].

3.3 Wear Tests

3.3.1 Friction Coefficient

Figure 3a–d shows the friction coefficient graphs of Mg–5Zn–1Y–xCa (x = 0–1 wt%) alloys in SBF as a function of time under the three loads of 10, 20, and 40 N. According to Fig. 3a, Mg–5Zn–1Y alloy shows almost similar and low friction coefficients of 0.13–0.30 under the experimented loads, although the alloy experiences the upper range of friction coefficient under 20 N load. It should be noted that the friction coefficient of Mg alloys is relatively low because of their hexagonal crystal structure which allow shearing on the basal planes [34]. Figure 3b displays the variation of the

Table 1 Chemical composition of the Mg–5Zn–1Y–xCa alloy (x = 0–1)

Alloy	Elements (wt%)								
	Zn	Y	Ca	Fe	Mn	Al	Cu	Si	Mg
Mg–5Zn–1Y	4.933	0.924	0.003	0.002	0.004	0.057	0.007	0.017	Bal.
Mg–5Zn–1Y–0.3Ca	4.696	0.815	0.281	0.002	0.004	0.058	0.007	0.010	Bal.
Mg–5Zn–1Y–0.5Ca	4.632	0.890	0.532	0.002	0.004	0.072	0.007	0.003	Bal.
Mg–5Zn–1Y–1Ca	4.540	0.905	1.036	0.002	0.004	0.067	0.007	0.007	Bal.

Fig. 1 SEM image of the microstructure of Mg–5Zn–1Y–xCa alloys; **a** x = 0, **b** x = 0.3, **c** x = 0.5, and **d** x = 1 wt%
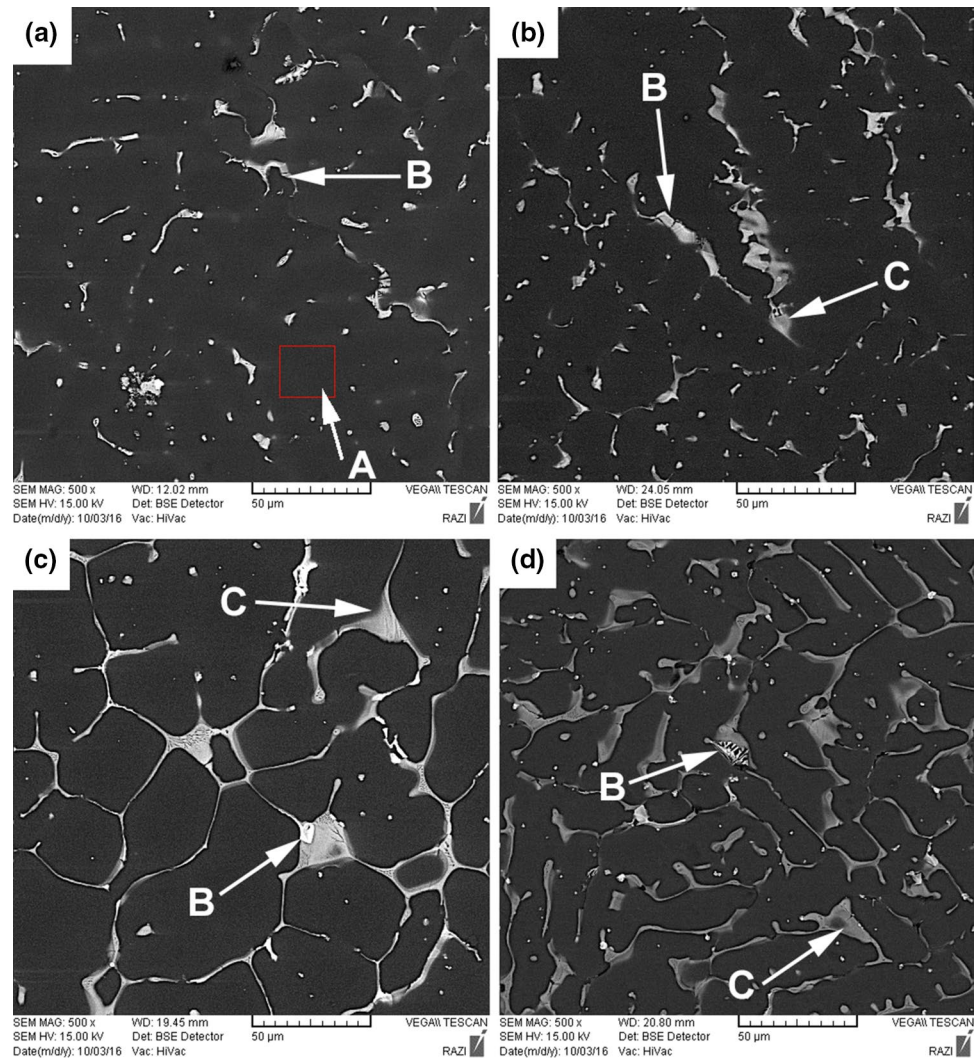

Table 2 EDS analysis of the microstructure constitutes of the alloys

Element	Point A		Point B		Point C	
	wt%	at%	wt%	at%	wt%	at%
Mg	95.1	98.2	34.5	59.8	46.2	61.9
Zn	4.4	1.7	54.1	34.8	17.6	8.8
Y	0.5	0.1	11.4	5.4	–	–
Ca	–	–	–	–	36.2	29.3

friction coefficient for Mg–5Zn–1Y–0.3Ca alloy. It is seen that the increase in wear load decreases the friction coefficient and the reduction rate is roughly the same for the load increment. The graphs reveal that the friction coefficient is in the range of 0.33 to 0.54 under the load of 10 N.

In contrast, it decreases to the range of 0.21 to 0.40 when the wear happens under the load of 20 N, while the friction coefficient decreases to almost a uniform value of 0.19 when the load increases to 40 N. The friction coefficient-time curves for Mg–5Zn–1Y–0.5Ca alloy is shown in Fig. 3c. It

indicates that the increase in wear load causes no significant changes in the behavior of friction coefficient, and the friction coefficient stands in the range of 0.24 to 0.3. Figure 3d represents a significant reduction in the friction coefficient of the Mg–5Zn–1Y–1Ca alloy when the wear load increases from 10 to 20 N. It is interesting to note that when the wear load is 10 N, the friction coefficient is between 0.33 and 0.52, while with it increases to 20 N, a significant decrease in the friction coefficient happens to reach between 0.15 and 0.26, although the increase in time has little effect on friction
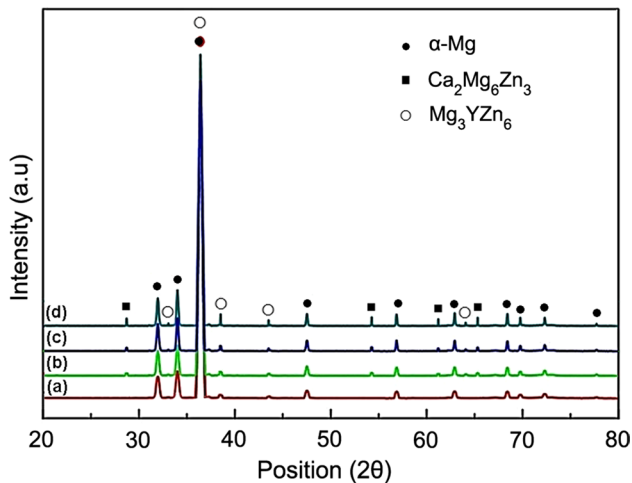
Fig. 2 XRD results of the cast Mg–5Zn–1Y–xCa alloys; **a** x = 0, **b** x = 0.3, **c** x = 0.5, and **d** x = 1 wt%

coefficient value. Further increase in wear load brings about no meaningful change in the friction coefficient.

Figure 4 represents the average friction coefficient for the studied alloys as a function of load. It can be seen that the increase in wear load decreases the friction coefficient in all alloys. However, the decrease is almost uniform for the 0.3 and 0.5 wt% Ca bearing alloys, while Ca-free alloy

shows a slight increase with increasing the wear load from 10 to 20 N, although the friction coefficient decreases to the lowest value, 0.17, when the wear load increases. In contrast, Mg–5Zn–1Y–1Ca alloy shows a remarkable decrease (52.5%) in friction coefficient when the load boosts from 10 to 20 N, yet it remains almost constant with further increase in wear load to 40 N. On the other hand, the friction coefficient experiences a significant increase (108%) reaching the highest value in the present study, at the wear load of 10 N, when Ca content increases to 1 wt%. Table 3 summarizes the results of wear rate and friction coefficient measurements.

3.3.2 Wear Rate

The values of volumetric wear rate of the alloys under different wear loads as a function of traveled distance are provided in Fig. 5. Table 3 summarizes the volumetric wear rates of the experimented alloys under various loads for 100 m. The data imply that the higher the wear load, the lower the wear rate for the alloys [35]. Figure 5 also shows that the wear rate variation of the alloys is uniform when the wear load increases. Figure 5a indicates that for the Ca-free alloy the maximum (0.0197 mm^3/N m) and minimum (0.0034 mm^3/N m) wear rates happen under the lowest (10 N) and the highest (40 N) loads, respectively, after conducting 20 m wear test. As the wear distance extends,
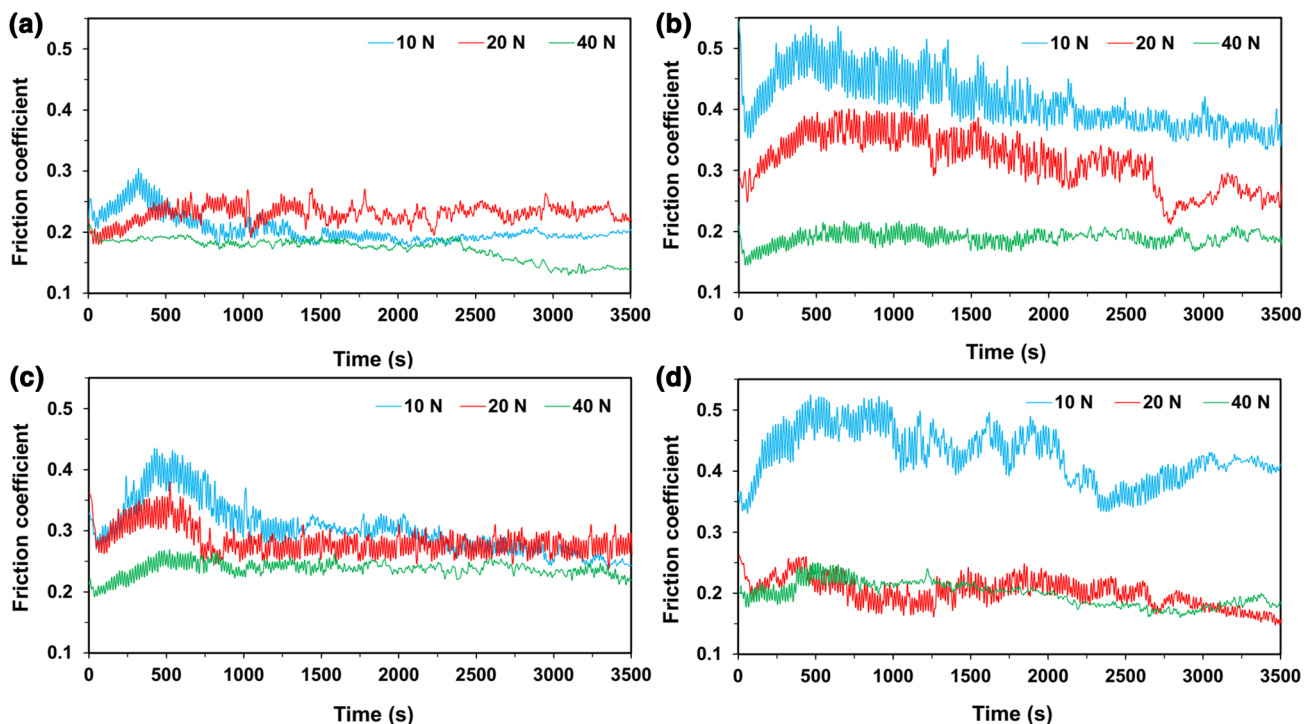

Fig. 3 Friction coefficient as a function of wear time under different wear loads for **a** Mg–5Zn–1Y, **b** Mg–5Zn–1Y–0.3Ca, **c** Mg–5Zn–1Y–0.5Ca, and **d** Mg–5Zn–1Y–1Ca alloys
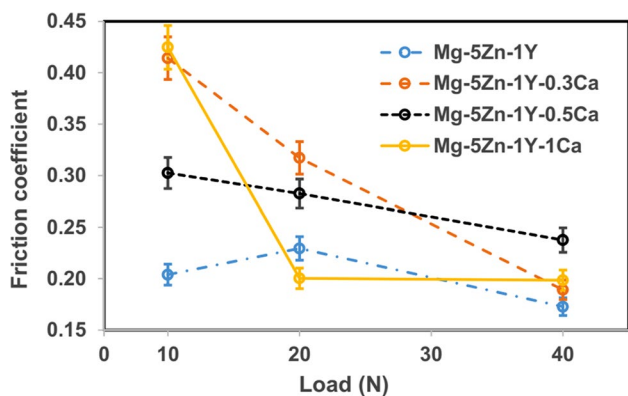
Fig. 4 The averaged friction coefficient for all samples as a function of loading

the wear rate does not considerably change, except for the load of 20 N, in which a slowly increasing trend is

seen in the wear rate, less than 10%, for the next whole wear length. Almost a similar behavior is observed for the 0.3 wt% (Fig. 5b) and 0.5 wt% (Fig. 5c) Ca bearing alloys throughout the wear traveled distance. In contrast, a different behavior is seen (Fig. 5d) when the Mg–5Zn–1Y–1Ca alloy is subjected to the wear test under the load of 10 N. In other words, a notable increase, approximately 70%, in wear rate happens for the whole wear distance under the load of 10 N, although no significant changes in the wear rate are seen for the other wear loads.

Figure 6 compares the wear rates of the alloys throughout 100 m traveling as a function of wear loads, implying that the wear rate of all alloys have a decreasing trend when the wear load increases. The graphs also indicate that the trend is quite similar for all alloys except the Mg–5Zn–1Y–1Ca alloy in which a prominent decrease (around 65%) in wear rate is seen when the load furthers from 10 to 20 N.

Table 3 The volumetric wear rate at 100 m as well as the average of friction coefficient of the experimented alloys under various loads

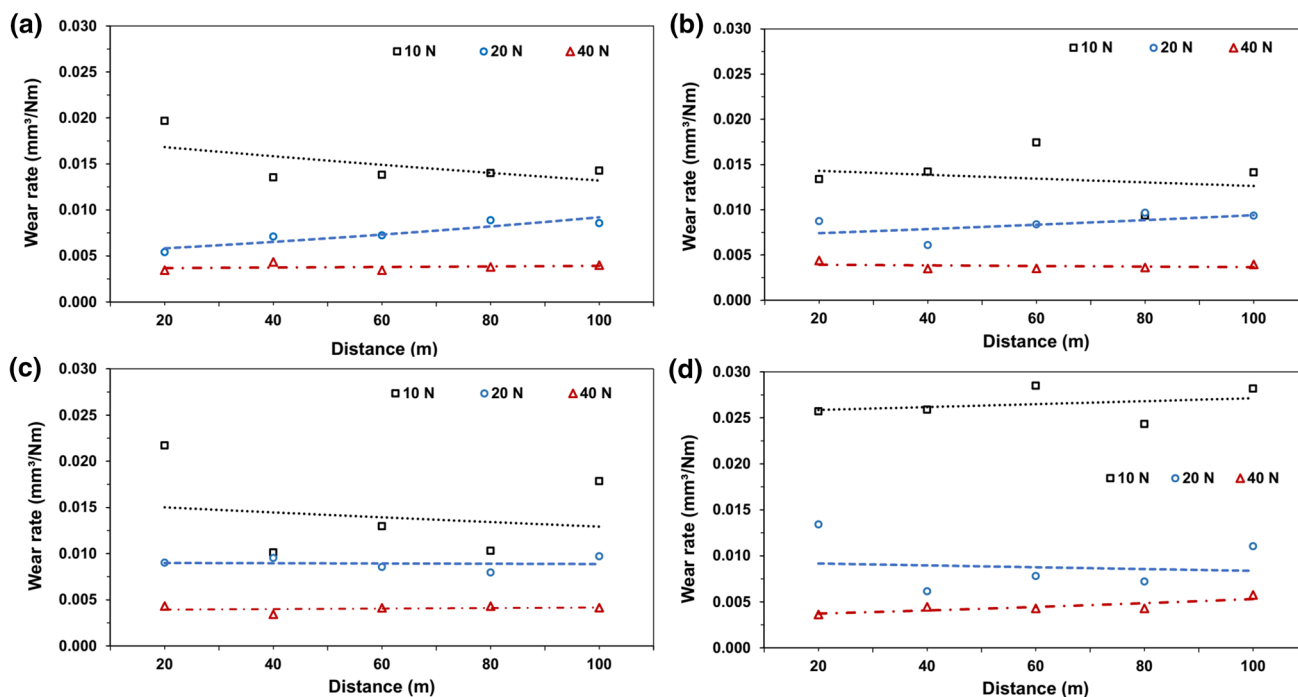| Alloy	ρ (g/cm^3)	Wear rate at 100 m			Average friction coefficient		
		10 N	20 N	40 N	10 N	20 N	40 N
Mg–5Zn–1Y	1.8210	0.0151	0.0074	0.0038	0.2039	0.2294	0.1728
Mg–5Zn–1Y–0.3Ca	1.8156	0.0137	0.0085	0.0038	0.4142	0.3172	0.1892
Mg–5Zn–1Y–0.5Ca	1.8113	0.0146	0.0089	0.0041	0.3025	0.2825	0.2376
Mg–5Zn–1Y–1Ca	1.8008	0.0265	0.0091	0.0045	0.4248	0.2003	0.1985

Fig. 5 Volumetric wear rate versus the distance under different loads for: **a** Mg–5Zn–1Y, **b** Mg–5Zn–1Y–0.3Ca, **c** Mg–5Zn–1Y–0.5Ca, **d** Mg–5Zn–1Y–1Ca
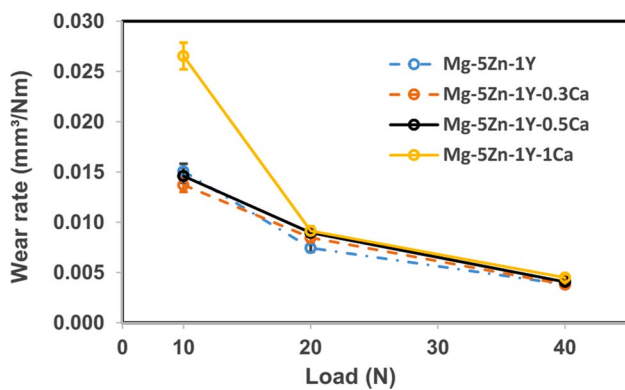
Fig. 6 The volumetric wear rate as a function of wear load

In contrast, the decrease for the other alloys is around 38%–51%, although uniformly decrease in wear rate (approximately 49%–55%) is observed in all alloys for further increase in wear load.

In addition to the determination of friction coefficient and wear rate, the changes in the area of wear zones are determined to complement the investigation. Figure 7 provides SEM images of the tip's surface of the pins under different wear loads.

It can be inferred that as the applied load increases, the area of the contact zone increases in contact mating surfaces. In other words, increasing wear load causes an enhancement in the area of the region affected by wear. This behavior is approved in the alloys with 0 and 0.5 wt% Ca. The approximate increase of values are 124% (from 38.190 to 85.613 μm^2) and 104% (from 56.795 to 115.695 μm^2) for the former and latter under the wear loads of 10 and 40 N, respectively. Similar behavior is seen in 0.3 and 1 wt% Ca bearing alloys in which the area of wear zones increases with the rising load from 10 to 20 N. However, further rising in wear load shows a decrease in the wear surface area. For instance, for the Mg–5Zn–1Y–0.3Ca alloy, after increasing the area of the contact zone for an approximate value of 54% (from 77.617 to 119.653 μm^2) under the loads of 10 N to 20 N, respectively, the surface area decrease to 79.642 μm^2 when the load is raised to 40 N. A comparable trend is established when Ca content increases to 1 wt%; an increase in the contact area from the approximate value of 80.466 to 87.230 μm^2 with rising wear load from 10 to 20 N, followed by a decrease in the area to an approximate value of 77.939 μm^2 after rising load to 40 N. The following reason is proposed for the reduction of wear rate with the load increment:

At the lower load, due to the lower contact area, enough amount of SBF solution penetrates into the gap between the pin and disk and causes the pin tip to corrode leading to the wear rate enhancement. In contrast, at the higher load, due to the wider contact interface, the amount of SBF penetrated

into the disk and pin interface is lower resulting in lesser corrosion damage and wear rate. In other words, it can be claimed that when the wear load is lower, the corrosion effect on the wear rate is greater than that of wear. Conversely, the wear shows a more pronounced effect on wear rate than the corrosion at the higher load.

3.4 Wear Mechanism

Due to the corrosive behavior of SBF and corrosion of the alloys throughout the wear test as well as the different microstructural characteristics of the alloys, it can be inferred that more than one mechanism is the cause of worn surfaces. Figure 8a–d show SEM images of the pins' surfaces worn under the load of 10 N. As can be seen on the images, low-stress scratches are formed on the surfaces, which are visible in the form of a series of pits in wear direction.

Figure 8b reveals that the scratches on the surface of the alloy containing 0.3 wt% Ca have a greater depth than those formed on the surface of other alloys, which can be attributed to the presence of hard particles between the contact mating surfaces. In addition, the light scratches on the worn surfaces may be formed due to the rubbing action of the particles detached from the contact surfaces. The particles may increase the friction coefficient in the abrasion mechanism, as Fig. 3b confirms. Therefore, for the alloy subjected to the wear test under the load of 10 N, the dominant wear mechanism is most probably abrasion.

SEM images of the worn surfaces of the studied alloys under the load of 20 N, shown in Fig. 9a–d, indicate parallel scratches in wear direction. The scratches are formed due to the penetration of hard protuberances of the opposite surface (hardened steel) forced against the soft surface of the pins or by the presence of intermetallic phases or residual particles removed from the surface of the alloys which trapped within the interface [36, 37]. These scratches represent the abrasive wear mechanism for removing the material from the surface. Figure 9a, SEM image of the worn surface of the Ca-free alloy, shows continuous deeper scratches than those formed on the worn surface of other alloys provided in Fig. 9. On the worn surface of the alloys containing 0.3 wt% (Fig. 9b) and 0.5 wt% Ca (Fig. 9c), the scratches are slight, while for the alloy containing 1 wt% Ca, except a deep scratch comprises several pits, other scratches are light (Fig. 9d). Therefore, it can be claimed that for the Ca-free alloy, the prime wear mechanism is most reasonably abrasion. Also, by increasing Ca content, the number and depth of scratches under the load of 20 N decrease, and the effect of abrasive wear mechanism reduces.

SEM images of the Mg–5Zn–1Y–(0–1)Ca alloys surfaces after wear test under 40 N load, demonstrated in Fig. 10, indicate different topographic qualities. The surfaces are well characterized with long scratches, especially in
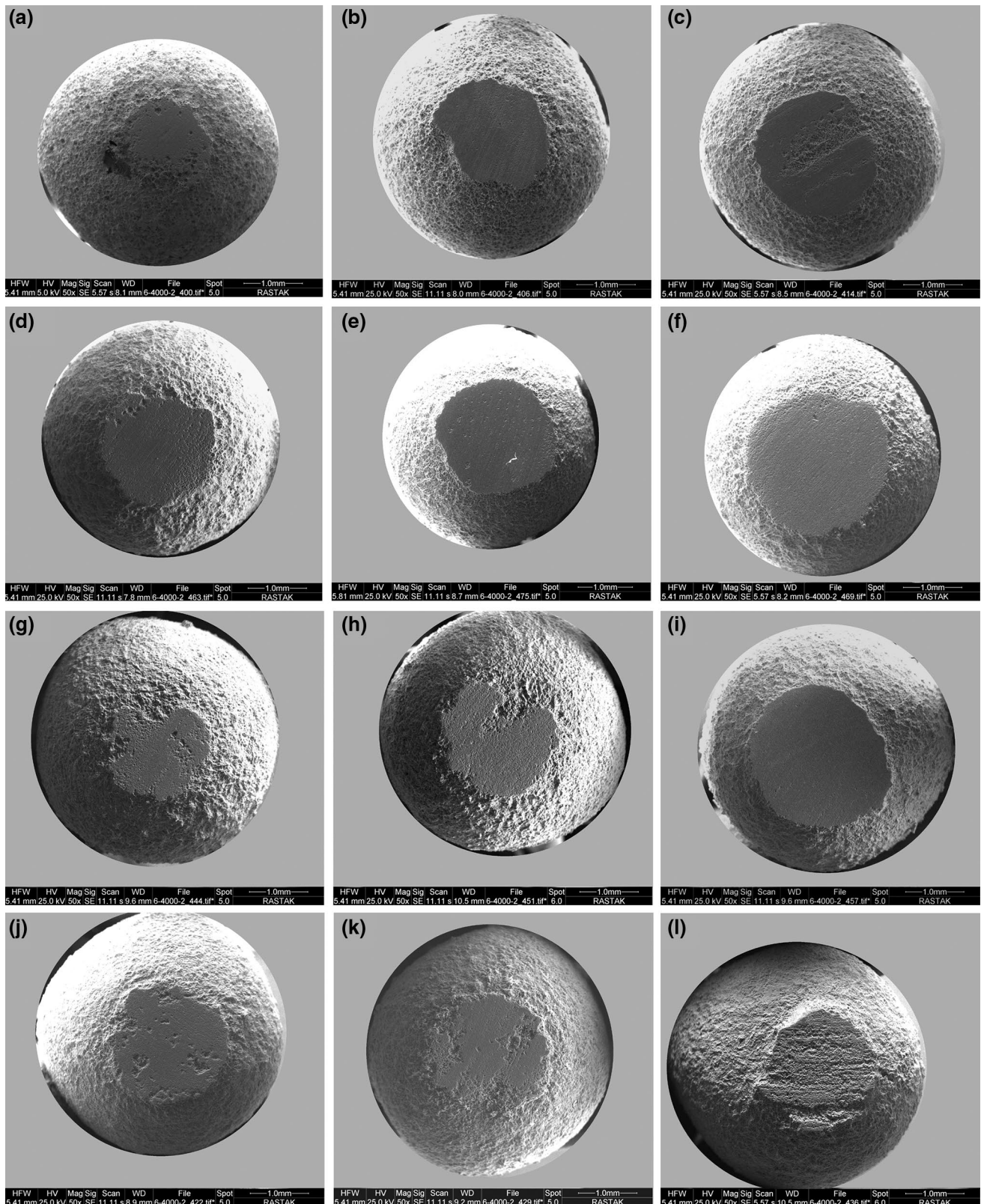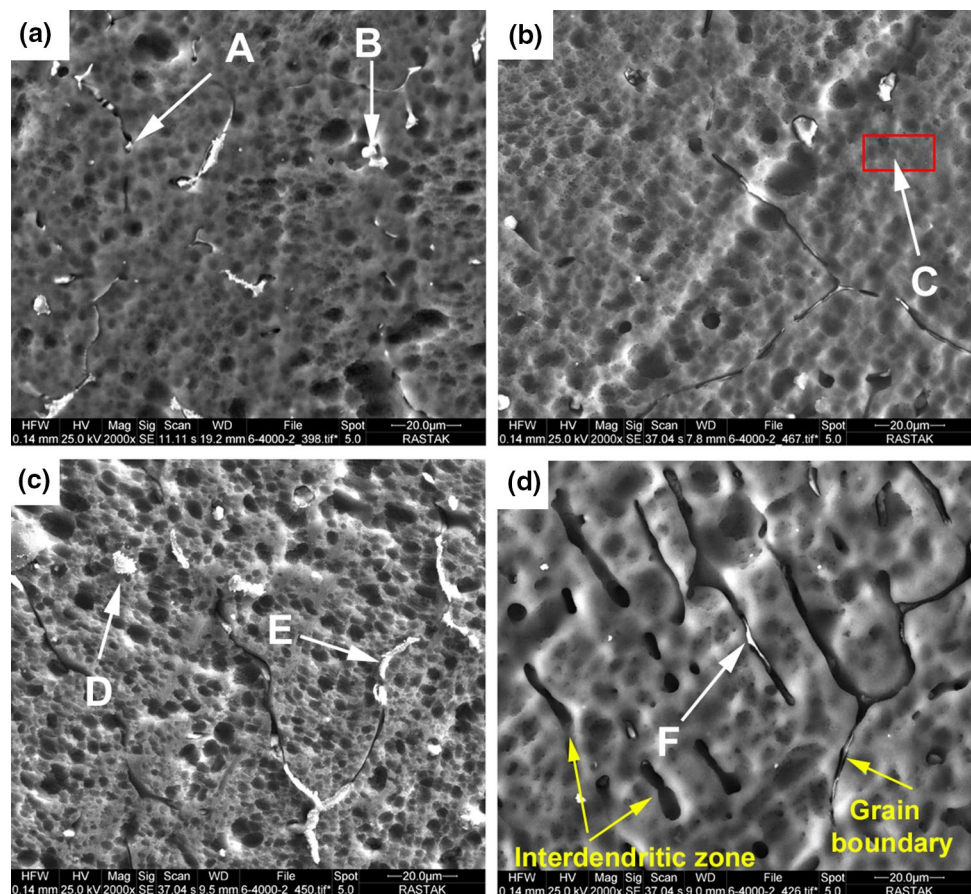
Fig. 7 SEM images of the tip's surface of the pins after the test under different wear loads; **a** 0 wt% Ca, 10 N, **b** 0 wt% Ca, 20 N, **c** 0 wt% Ca, 40 N, **d** 0.3 wt% Ca, 10 N, **e** 0.3 wt% Ca, 20 N, **f** 0.3 wt% Ca, 40 N, **g** 0.5 wt% Ca, 10 N, **h** 0.5 wt% Ca, 20 N, **i** 0.5 wt% Ca, 40 N, **j** 1 wt% Ca, 10 N, **k** 1 wt% Ca, 20 N, and **l** 1 wt% Ca, 40 N

Fig. 8 SEM micrographs of the worn surfaces of the Mg–5Zn–1Y–xCa alloys under the load of 10 N; **a** x = 0, **b** x = 0.3, **c** x = 0.5, and **d** x = 1 wt%
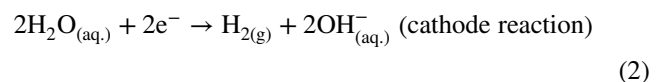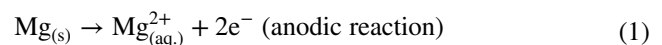

0–0.5 wt% Ca containing alloys, which the abrasion seems to be the dominant mechanism in the alloys. Therefore, considering the above results, it can be claimed that, abrasion is the dominant wear mechanism in all alloys, and it appears to be more severe in Mg–5Zn–1Y–0.3Ca alloy especially when the load is 40 N.

The results of EDS analysis given in Table 4 confirm the presence of chromium (Cr) on the surface of the alloys. The presence of hard intermetallic phases of the experimented alloys remained from the wear action and corrosion attack, occurred due to the high corrosiveness of SBF, can be the probable reason to remove Cr carbide particles from the steel surface, and permanently transfer them to the surface of the alloys. Based on the EDS results, this phenomenon is more evident in Ca-free alloy under the loads of 10 and 20 N (Points A and G), and in 0.5 wt% Ca bearing alloy under 10 and 40 N loads (Points E and L).

4 Discussion

The corrosion attack to the surface involves electrochemical reactions of oxide and hydroxide products and H_2 gas. Corrosion reactions of Mg and its alloys include anodic and cathodic reactions. Exposing Mg-based alloys to SBF results in the dissolution of Mg to convert into Mg^{2+} through the anodic reaction (1); in the meantime, the cathode reaction (2) releases H_2 gas due to galvanic corrosion [38, 39].

$$Mg_{(s)} \rightarrow Mg^{2+}_{(aq.)} + 2e^- \text{ (anodic reaction)} \quad (1)$$

$$2H_2O_{(aq.)} + 2e^- \rightarrow H_{2(g)} + 2OH^-_{(aq.)} \text{ (cathode reaction)} \quad (2)$$

Afterwards, Mg^{2+} reacts with OH^- to form $Mg(OH)_2$ on the surface of Mg alloy (reaction 3) [38, 39].

$$Mg^{2+}_{(aq.)} + 2OH^- \rightarrow Mg(OH)_{2(s)} \quad (3)$$
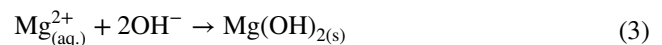
Due to the formation of non-homogeneous porous $Mg(OH)_2$ layer, the corrosion rate of the alloy is reduced. The presence of chloride ion in SBF leads to the reaction (4) and production of corrosion pits [8] on the surface of the pins and participation of the corrosion products on the mating surfaces.

$$Mg(OH)_{2(s)} + 2Cl^-_{(aq.)} \rightarrow MgCl_{2(aq.)} + 2OH^-_{(aq.)} \quad (4)$$
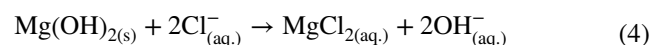
Considering the presence of other onions like phosphates, carbonates, and sulphates in the SBF, other reactions may

Fig. 9 SEM micrographs of the worn surfaces of the Mg–5Zn–1Y–xCa alloys under the load of 20 N; **a** x = 0, **b** x = 0.3, **c** x = 0.5, and **d** x = 1 wt%
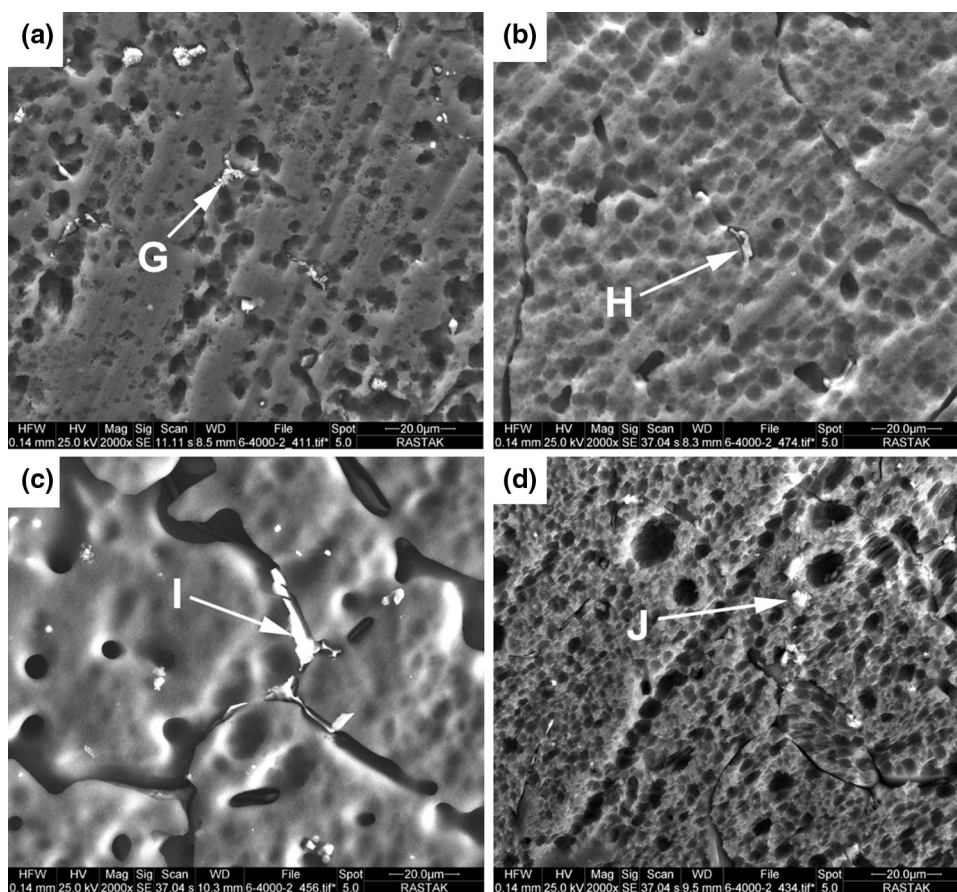
occur, leading to the formation of more products. However, considering the low amount of the onions and, on the other hand, high concentration of the chloride ion, it is considered as the main ion to attack $Mg(OH)_2$ layer and contribute to the enhancement of problem.

As mentioned in Sect. 3.2 (Microstructural analysis) the microstructure of Ca-free alloy contains α-Mg solid solution matrix and intermetallic Mg_3YZn_6. With the addition of Ca to the alloy, another intermetallic phase, $Ca_2Mg_6Zn_3$, is also formed, and its quantity increases by increasing the Ca content and forms a network along grain boundary (Fig. 1). Therefore, a severe potential difference is developed between the matrix (anode) and the intermetallic phases (cathode). It causes the formation of micro galvanic cells resulting in corrosion damage of the matrix; the more the Ca content, the higher the severe corrosion attack [39]. The consequence of this behavior can be clearly distinguished in the SEM images of the alloys for all wear loads (Figs. 8, 9, 10). Furthermore, in addition to corrosion attack, the wear mechanism concurrently removes material from the surface, leading to a further volume reduction of the alloys [40]. In other words, increasing Ca amount results in more volume reduction of the alloys due to the simultaneous action of corrosion and wear phenomena. The corrosion of the alloys in the SBF

produces the protective film of $Mg(OH)_2$ on the surface. However, due to the friction created between the pin and disk surfaces during the wear process, the film is broken and migrate toward the surrounding wear zone. As a result, the alloy substrate is exposed to the SBF, consequently, corrosion and wear damages continue. Therefore, continuous formation and removal of the protective layer are another reason for continuously decreasing and increasing the friction coefficient [41] confirming the instability of the coefficient in the wet wear test (Fig. 3). Subsequently, the formation of the film increases the wear resistance by reducing the friction coefficient. Also, rubbing the alloys surfaces is facilitated under the SBF environment. On the other hand, the wear damage is accelerated due to the corrosion effect in the SBF. Therefore, the wet wear rates of the alloys, which are accompanied by the formation of corrosion products, is usually high in the course of wear process. In other words, the increase in the wet wear rate of each pin is either due to the removal of material from the surface by wear, or the removal of corrosion products formed on the surface. The results of the present study are in good consistent with those reported by other researchers [26, 31]. It is worth noting that the corrosion is also intensified by wear effect.

Fig. 10 SEM micrographs of the worn surfaces of the Mg–5Zn–1Y–xCa alloys under the load of 40 N; **a** x = 0, **b** x = 0.3, **c** x = 0.5, and **d** x = 1 wt%
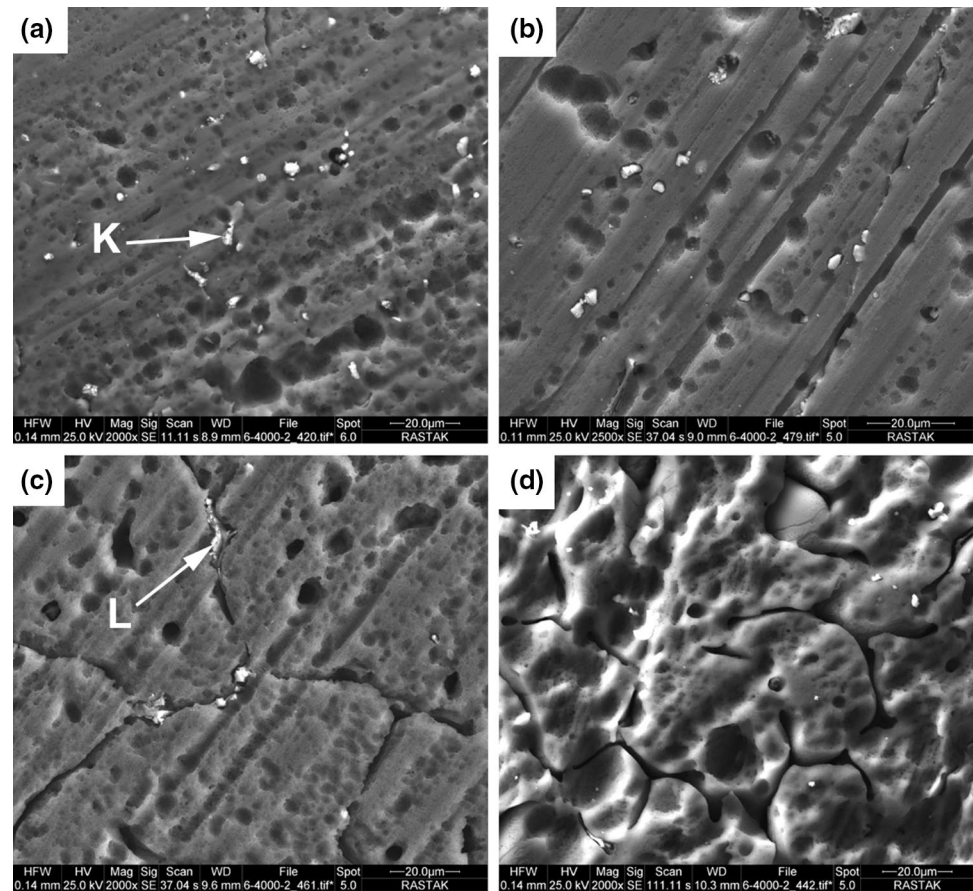

Table 4 EDS analysis results of different locations marked on Figs. 8, 9 and 10

Element	Chemical composition (wt%)											
	A	B	C	D	E	F	G	H	I	J	K	L
Mg	62.7	68.9	94.6	73.9	39.7	78.3	55.5	59.4	59.4	54.6	74.7	61.4
Zn	12.4	29.9	4.8	8.9	24.3	14.7	12.7	28.8	23.8	22.2	14.3	9.8
Y	3.6	1.2	0.3	0.8	14.8	6.2	3.9	11.5	16.9	17.2	4.7	2.5
Ca	–	–	0.3	2.6	0.4	0.2	–	0.3	0.2	0.7	–	0.4
Cr	21.3	–	–	13.8	20.8	–	27.9	–	–	5.3	6.3	25.9

Taking a look at the curves in Fig. 3, it can be found out that the fluctuations of the friction coefficient at the low loads, in the course of wear test increase. On the contrary, the more the wear load, the lower the fluctuation. The fluctuation is intensified when the alloy contains Ca; the Ca-free alloy shows the least fluctuation. The increase in Ca content to 0.3 wt%, and consequently, the emergence of more intermetallic particles on the surface (Fig. 1b) not only leads to higher fluctuations but causes an increase in the friction coefficient. However, the fluctuations decrease when Ca content increases to 0.5 wt%, which can be attributed to the intermetallic particles continuity (Fig. 1c) as well as tougher removing the particles from the surface. Subsequently, increasing Ca content to 1 wt%, due to the formation of

further hard intermetallic particles on the surface (Fig. 1d), the friction coefficient increases under low load.

Through observing the SEM images (Fig. 8), it is realized that abrasive wear is well dominated in the Mg–5Zn–1Y–0.3Ca alloy under 10 N load. Moreover, the deep pits, corroded grain boundaries as well as interdendritic spaces on the surface of Mg–5Zn–1Y–1Ca alloy (Fig. 8d) indicate an intensive degradation of the alloy in the SBF, which is in agreement with those reported by Naghdali et al. [22]. Also, the intermetallic phases can clearly be seen embedded in the spaces (point F in Fig. 8d) left after the wear and corrosion processes. In contrast, the low values and uniformity of the friction coefficient (Fig. 3a) and wear rate (Fig. 5a) curves of the Ca-free alloy represent a better

wear resistance compared with those containing higher Ca. This may be due to the better performance of the Mg(OH)$_2$ protective layer, formed between the contacting pair surfaces and acts as a lubricant on the surface. Furthermore, due to the uniformity of surface (Fig. 8a–c) and the low wear rates (Fig. 6), it can be concluded that, under the load of 10 N, the wear resistance of the alloys with low content of Ca (up to 0.5 wt%) is better than that of contains high Ca (1 wt%). In other words, the wear resistance of Mg–5Zn–1Y–xCa decreases with increasing Ca content under 10 N wear load.

The SEM micrographs shown in Fig. 9 reveals the occurrence of a similar wear mechanism under the load of 20 N. The scratches on the surface (Fig. 9a) proposes the incidence of abrasive wear in Ca-free alloy. In addition, some grooves have formed through joining corrosion pits together. With the addition of Ca content to 0.3 and 0.5 wt%, the enhanced corrosion of the matrix adjacent to the grain boundary contributes detaching the secondary phases from the boundary by wear mechanism. It should be noted that the removed phases may be trapped in the corroded areas in the course of wear test, as denoted by Point I in Fig. 9c.

Increasing wear load to 20 N, shows a similar behavior. As Fig. 6 reveals, increasing Ca content results in deterioration of wear resistance; therefore, the wear behavior of the Mg–5Zn–1Y–xCa under the load of 20 N is almost similar to that of the 10 N, and the Ca-free alloy shows the highest wear resistance in SBF. As the SEM image in Fig. 10a shows, the presence of scratches formed by the accumulation of pits, secondary phase and particles seen in light color, as well as large pits on the surface of Mg–5Zn–1Y alloy indicate the probable occurrence of different wear mechanism, although the abrasion may be the more pronounced one under the load of 40 N. Figure 10b, c reveals that abrasion is again the dominant wear mechanism happens on the surface of 0.3 and 0.5 wt% Ca bearing alloys. The continuous deep scratches on the surface created by rubbing the hard debris on the surface are well represented. In the alloy containing 1 wt% Ca, due to the presence of a significant number of pits (Fig. 10d), it can be claimed that in addition to abrasive wear mechanism corrosion phenomenon also occurs. Moreover, the presence of Cr content particles on the surface (Table 4) proposes removing Cr carbide particles from the surface of the hardened steel disc which contributes to the abrasion of the surface. Therefore, increasing Ca content beyond 0.3 wt%, the wear resistance of the alloy reduces due to the existence of wear together with the corrosion process which approves the results given in Fig. 6. In other words, at the load of 40 N, the alloy with the lowest Ca content have the highest wear resistance. In general, it can be claimed that by increasing the wear load, although the abrasion mechanism is enhanced in the Ca-free, 0.3 and 0.5 wt% Ca containing alloys, the wear rate of the alloys reduces. Also, Mg–5Zn–1Y–1Ca alloy, due to the higher

corrosion rate [42], shows higher wear rate under low load; however, higher loads restrict more SBF to reach the pin surface, and corrosion is confined causing the alloy follows the wear rate as the other alloys.

5 Conclusions

In this study, the friction coefficient and the wear rate of the biodegradable Mg–5Zn–1Y–xCa (x = 0–1 wt%) alloys are investigated in the simulated body fluid under loads of 10 to 40 N. The following conclusions are obtained:

1. Increasing Ca content decreases wear resistance. With the increase in wear load, in addition to the friction coefficient, the wear rate of the alloys reduces. Ca-free alloy shows the highest wear resistance under all experimented loads.
2. Ca-free alloy shows the lowest friction coefficient under the highest wear load; while Mg–5Zn–1Y–1Ca alloy has the highest friction coefficient under the least wear load.
3. Although SBF is expected to play as a lubricant and reduces the friction coefficient, corrosion of all alloys in this environment increases the wear rate.
4. Abrasion is the dominant wear mechanism in all alloys, and it is intensified on the surface of Mg–5Zn–1Y–0.3Ca alloy under higher loads.

References

1. L. Cui, L. Sun, R. Zeng, Y. Zheng, S. Li, Sci. China Mater. **61**, 607 (2018)
2. K.K. Ajith Kumar, U.T.S. Pillai, B.C. Pai, M. Chakraborty, Met. Mater. Int. **19**, 1167 (2013)
3. L. Tonelli, P. Dolcet, M. Dabal, C. Martini, Wear **404–405**, 122 (2018)
4. S. Koleini, M. Hasbullah Idris, H. Jafari, Mater. Des. **33**, 20 (2012)
5. F. Qin, G. Xie, Z. Dan, Sh Zhu, I. Seki, Intermetallics **42**, 9 (2013)
6. J. Mol, Asp. Med. **24**, 27 (2003)
7. J.Z. Ilich, J.E. Kerstetter, J. Am. Coll. Nutr. **19**, 715 (2000)
8. F. Witte, V. Kaese, H. Haferkamp, E. Switzer, A. Meyer-Lindenberg, C.J. Wirth, Biomaterials **26**, 3557 (2005)
9. A. Madhan Kumar, S. Fida Hassan, A.A. Sorour, M. Paramsothy, M. Gupta, Met. Mater. Int. **25**, 105 (2009)
10. N. Li, Y. Zheng, J. Mater. Sci. Technol. **29**, 489 (2013)
11. B. Zhang, Y. Hou, X. Wang, Y. Wang, L. Geng, Mater. Sci. Eng. C **31**, 1667 (2011)
12. R. Erbel, C. Di Mario, J. Bartunek, J. Bonnier, B. de Bruyne, F.R. Eberli, P. Erne, M. Haude, B. Heublein, M. Horrigan, C. Ilsley, D. Bose, J. Koolen, T.F. Luscher, N. Weissman, R. Waksman, Lancet **369**, 1869 (2007)

13. B. Smola, L. Joska, V. Březina, I. Stulíková, F. Hnilica, Mater. Sci. Eng. C **32**, 659 (2012)
14. H. Tapiero, K.D. Tew, Biomed. Pharmacother. **57**, 399 (2003)
15. L. Cizek, S. Rusz, O. Hilser, R. Śliwa, D. Kuc, T. Tanski, M. Tikocz, Arch. Metall. Mater. **62**, 2365 (2017)
16. S. Cai, T. Lei, N. Li, F. Feng, Mater. Sci. Eng. C **32**, 2570 (2012)
17. S. Zhang, X. Zhang, C. Zhao, J. Li, Y. Song, C. Xie, H. Tao, Y. Zhang, Y. He, Y. Jiang, Y. Bian, Acta Biomater. **6**, 626 (2010)
18. Y. Sun, B. Zhang, Y. Wang, L. Geng, X. Jiao, Mater. Des. **34**, 58 (2012)
19. Y. Jang, Z. Tan, Ch. Jurey, Zh Xu, Zh Dong, B. Collins, Y. Yun, J. Sankar, Mater. Sci. Eng. C **48**, 28 (2015)
20. V. Neubert, I. Stulíková, B. Smola, B.L. Mordike, M. Vlach, A. Bakkar, J. Pelcová, Mater. Sci. Eng. A **462**, 329 (2007)
21. E. Zhang, W. He, H. Du, K. Yang, Mater. Sci. Eng. A **488**, 102 (2008)
22. S. Naghdali, H. Jafari, M. Malekan, Thermochim. Acta **667**, 50 (2018)
23. MZh Ge, J.Y. Xiang, Y. Tang, X. Ye, Z. Fan, Y.L. Lu, X.H. Zhang, Surf. Coat. Technol. **337**, 501 (2018)
24. J. An, R.G. Li, Y. Lu, C.M. Chen, Y. Xu, X. Chen, L.M. Wang, Wear **265**, 97 (2008)
25. Y. Niu, R. Cui, Y. He, Z. Yu, J. Alloys Compd. **610**, 294 (2014)
26. D.B. Liu, B. Wu, X. Wang, M.F. Chen, Rare Met. **34**, 553 (2015)
27. H. Somekava, A. Shimoda, T. Hirayama, T. Matsuoka, T. Mukai, Mater. Trans. **55**, 216 (2014)
28. N.N. Aung, W. Zhou, L.E.N. Lim, N.N. Aung, W. Zhou, L.E.N. Lim, Wear **265**, 780 (2008)
29. C. Taltavull, P. Rodrigo, B. Torres, A.J. López, J. Rams, Mater. Des. **56**, 549 (2014)
30. C. Taltalvull, B. Torres, A.J. López, J. Rams, Wear **301**, 615 (2013)
31. H. Li, D.B. Liu, Y. Zhao, F. Jin, M.F. Chen, J. Mater. Eng. Perform. **25**, 3890 (2016)
32. H. Jafari, F. Rahimi, Z. Sheikhsofla, Mater. Corros. **67**, 396 (2015)
33. M.L. Hu, Q.D. Wang, C.J. Chen, D.D. Yin, W.J. Ding, Z.S. Ji, Mater. Des. **42**, 223 (2012)
34. G. Peitao, T. Mingyang, Z. Chaoyang, Surf. Coat. Technol. **359**, 197 (2019)
35. J. Dai, X. Zhang, Q. Yin, Sh Ni, Zh Ba, Zh Wang, J. Magn. Alloy **5**, 448 (2017)
36. A. Somi Reddy, B.N. Pramila Bai, K.S.S. Murthy, S.K. Biswas, Wear **181–183**, 658 (1995)
37. B.N. Pramila Bai, S.K. Biswas, Acta Metall. Mater. **39**, 833 (1991)
38. N.V. Phuong, B.R. Fazli, S. Moon, Met. Mater. Int. **23**, 106 (2017)
39. M. Bornapour, M. Celikin, M. Cerruti, M. Pekguleryuz, Mater. Sci. Eng. C **35**, 267 (2014)
40. V. Kumar, L. Li, H. Gui, X. Wang, Q.X. Huang, Q.Y. Li, F. Mokdad, D. Chen, D.Y. Li, Wear **414–415**, 126 (2018)
41. F. Muhaffel, H. Cimenoglu, Surf. Coat. Technol. **357**, 822 (2019)
42. F. Doost Mohammadi, H. Jafari, Trans. Nonferr. Met. Soc. China **28**, 2199 (2018)

Publisher's Note Springer Nature remains neutral with regard to jurisdictional claims in published maps and institutional affiliations.